# Nanoparticle localization within chiral liquid crystal defect lines and nanoparticle interactions

Mykola Tasinkevych [1,2,3,*] Sungoh Park,[4] Haridas Mundoor,[4] and Ivan I. Smalyukh[3,4,5,†]

[1]*SOFT Group, School of Science and Technology, Nottingham Trent University, Clifton Lane, Nottingham NG11 8NS, United Kingdom*
[2]*Departamento de Física, and Centro de Física Teórica e Computacional, Faculdade de Ciências, Universidade de Lisboa, 1749-016 Lisboa, Portugal*
[3]*International Institute for Sustainability with Knotted Chiral Meta Matter, Hiroshima University, Higashihiroshima 739-8511, Japan*
[4]*Department of Physics, University of Colorado, Boulder, Colorado 80309, USA*
[5]*Soft Materials Research Center; Department of Electrical, Computer, and Energy Engineering and Materials Science and Engineering Program; and Renewable and Sustainable Energy Institute, National Renewable Energy Laboratory, University of Colorado, Boulder, Colorado 80309, USA*

Self-assembly of colloidal particles into predefined structures is a promising way to design inexpensive manmade materials with advanced macroscopic properties. Doping of nematic liquid crystals (LCs) with nanoparticles has a series of advantages in addressing these grand scientific and engineering challenges. It also provides a very rich soft matter platform for the discovery of unique condensed matter phases. The LC host naturally allows the realization of diverse anisotropic interparticle interactions, enriched by the spontaneous alignment of anisotropic particles due to the boundary conditions of the LC director. Here we demonstrate theoretically and experimentally that the ability of LC media to host topological defect lines can be used as a tool to probe the behavior of individual nanoparticles as well as effective interactions between them. LC defect lines irreversibly trap nanoparticles enabling controlled particle movement along the defect line with the use of a laser tweezer. Minimization of Landau–de Gennes free energy reveals a sensitivity of the ensuing effective nanoparticle interaction to the shape of the particle, surface anchoring strength, and temperature, which determine not only the strength of the interaction but also its repulsive or attractive character. Theoretical results are supported qualitatively by experimental observations. This work may pave the way toward designing controlled linear assemblies as well as one-dimensional crystals of nanoparticles such as gold nanorods or quantum dots with tunable interparticle spacing.

## I. INTRODUCTION

Introduced by Einstein within his celebrated theory of Brownian motion [1], the colloidal atom paradigm has provided motivation and means for organizing particles into crystals and other structures mimicking and even exceeding the structural diversity of molecular and atomic systems [2]. Liquid crystal (LC) colloids [3–5] have a series of advantages in addressing these grand scientific and engineering challenges, offering a means of controlling particle self-assembly via changing the particles' surface boundary conditions [6], shape [7], topology [8], and chirality [9]. Colloidal particles distort preferred uniform alignment of LC molecules and tend to adopt the LC free-energy minimizing configurations.

For dilute colloidal systems, the effective LC-mediated interactions can be described in terms of an elastic multipole expansion [10–14], in an analogy with the electrostatics. Colloidal particles inducing elastic distortions with the leading dipolar [10,15], quadrupolar [15], and even higher-order hexadecapolar [16,17] symmetries have been realized experimentally. The elastic multipole formalism provides a satisfactory description of interactions in nematic colloids at large separations, whereas near-field LC distortions are governed by highly nonlinear differential equations and often contain point or line topological defects [3,10,15,18] in the vicinity of the colloidal particles. When two such defect-decorated colloidal particles are brought together, a valencelike colloidal bonding realized via sharing of topological defects between colloidal particles has been demonstrated in Refs. [3,18]. This defect-bonding mechanism is an analog of covalent bonding between atoms where the topological defects play the role of the valence electrons and may be exploited to better control the process of colloidal self-assembly [10].

Experimentally, some two-dimensional (2D) [15] as well as three-dimensional (3D) [19] colloidal crystallites have been previously reported relying, however, on laser-tweezer-assisted assembly rather than on self-assembly alone. As a result, only crystallites with sizes up to several unit cells could be built up.

The recent advent of charged nematic nanocolloids [20] has set the self-assembling potential of these systems on a qualitatively unique level, enabling spontaneous formation of low-symmetry nanoparticle crystals [20] and mesophases [21–23] such as ferromagnetic fluids [21,23], orthorhombic biaxial nematics [22], and even triclinic colloidal crystals with ultralow nanoparticle packing fractions [20]. These

---

*[*]mykola.tasinkevych@ntu.ac.uk
[†]ivan.smalyukh@colorado.edu

low-symmetry colloidal crystals, with micrometer-range unit cells, self-assemble due to a fine interplay between highly anisotropic LC-mediated interactions and electrostatic repulsive forces. Furthermore, the temperature and electric-field dependence of the various nanoparticle interactions enables the realization of ferroelectric and dielectric molecular-nanoparticle fluids with different point group symmetries as well as their real-time reversible reconfiguration [24,25].

An exciting opportunity for controlling individual nanoparticles and small-number assemblies of them is provided if one explores a natural tendency of LC to host disclination lines. These topological line defects can be used to control self-assembly of amphiphilic molecules, trap quantum dots, plasmonic gold, and other nanoparticles along two dimensions, but allow for controlled movement of these particles along the defect line [25–32]. The nanoparticles can be moved along the defect line by using infrared laser tweezers and can be optically manipulated [26]. This enables exploration of the properties of nanoparticles and interactions between them at a single particle level or at the level of a few nanoparticles. This strategy was pursued in [26] which discusses the behavior of nematic colloids formed by ferroelectric nanoplatelets. Confinement of the nanoparticles within singular defect lines allowed probing a delicate interplay of long-range electrostatic interactions and shorter-range quadrupolar-type interactions due to the LC's orientational elasticity. Additionally, it was shown that electrostatic dipoles allow for a facile reconfiguration of LC colloidal behavior, with the interparticle distances an order of magnitude larger than the nanoparticle size controllable by a vanishingly weak electric field. On the other hand, it was found that nanoparticles entrapped within defect lines can exhibit elastic monopole moments [33], which in the nematic bulk of uniformly aligned far-field background could be found only in the presence of elastic torques due to external stimuli such as light [34].

Here, we investigate the interactions between nanoparticles entrapped in the line defects theoretically, focusing on the effects of the particle shapes, the strength of particle surface anchoring, and temperature. While focusing on twist disclinations as entrapping defects for one-dimensional confinement, differently from the prior literature discussed above, we explore the role of particle shape in dimensions in defining colloidal self-assembly and interactions. We obtain director configurations around the particles in the presence of the line defect by using the Landau–de Gennes free-energy approach [35]. Several theoretical predictions concerning the nanoparticle interactions are confirmed experimentally. In the next section we describe the experimental and numerical methods. In the Results section we discuss effective pair interaction between nanoparticles of the following shapes: sphere, cuboid, spherocylinder, and square platelets. The last section presents the Conclusions and outlook.

## II. MATERIALS AND METHODS

### A. Sample preparation and experimental methods

The nanoparticles used for the experiments were chemically synthesized following the procedures described before. Upconversion nanorods (20 nm × 1.6 μm) and nanocubes (size ≈20 nm) of NaYF$_4$, were prepared by the hydrothermal synthesis route [36,37]. Silica capped gold nanorods (GNRs) of size ≈40 × 60 nm were synthesized following the seed-mediated synthesis followed by the hydrolysis reaction for silica growth [38]. Nanoplatelets of cadmium selenide (CdSe) were synthesized following the synthesis route reported earlier [39]. The nanorods and nanocubes were designed to exhibit upconversion luminescence in the visible region when excited with a 980 nm light [36]. The chiral nematic LCs used for the experiments were prepared by doping a commercially available nematic mixture E7 with a chiral dopant cholesteryl pelargonate (Sigma-Aldrich), to yield a desired cholesteric pitch ∼12 μm. Very dilute dispersions of nanoparticles in chiral nematic LC were prepared by mixing a nanoparticle dispersion in ethanol with LC followed by solvent evaporation at 70 °C and quenching to nematic phase under vigorous mechanical agitation. The LC dispersions were infiltrated into a glass cell by means of capillary forces and sealed using fast-setting epoxy. The glass cells of ∼10 μm spacing were prepared by sandwiching two glass plates with glass fiber segments mixed in a UV-curable glue. The inner surfaces of the glass plates were treated with DMOAP, which promotes the strong homeotropic boundary conditions for the LC molecules at the surface of the glass plates.

The optical microscopy characterization of nanoparticles in the line defect was performed using a confocal microscopy setup (FV 300, Olympus) built around an inverted microscope (Olympus IX 81), equipped with light sources, polarizers, high-magnification objectives, and laser sources for optically exciting the particles. The microscope is integrated with a holographic optical tweezer, using the output from a fiber laser operating at 1064 nm. The optical micrographs of the nanoparticles and LC line defects in the dark-field and bright-field modes were collected using a color CCD camera (Flea-Col, Point Grey), and for the luminescence-based confocal microscopy characterization of the nanoparticles trapped in the line defect, the particles were excited with either 488 nm output from an argon-ion laser or 980 nm output from a Ti:sapphire oscillator (Coherent, Chameleon Ultra).

The interaction potential between two GNR particles in the line defect was characterized based on the variation of interparticle spacing with time when they are moved close to each other with the help of an optical tweezer and released. The interparticle spacing between the GNR particles was extracted from the video microscopy using image processing software (IMAGEJ v1.51).

### B. Landau–de Gennes free-energy and numerical approach

The Landau–de Gennes phenomenological description is based on a traceless, symmetric rank-3 tensorial order parameter $Q_{ij}$ ($i, j = 1, \ldots, 3$), which has five independent components. In the one elastic constant approximation, the Landau–de Gennes free energy of a representative chiral nematic may be written as [40,41]

$$F_{\text{LdG}} = \int_V \left[ AQ_{ij}^2 - BQ_{ij}Q_{jk}Q_{ki} + C\left(Q_{ij}^2\right)^2 + \frac{L_1}{2}\partial_k Q_{ij}\partial_k Q_{ij} \right.$$
$$\left. + \frac{L_2}{2}\partial_j Q_{ij}\partial_k Q_{ik} + \frac{4\pi L_1}{P}\epsilon_{ijk}Q_{il}\,\partial_j Q_{kl} \right] dV, \qquad (1)$$

where $A$, $B$, $C$ are phenomenological material constants; $L_1$, $L_2$ are phenomenological parameters related to the Frank elastic constants; and $P$ is the cholesteric pitch. $\epsilon_{ijk}$ is the Levi-Civita symbol, and the Einstein convention for summation over repeated indices is implied. The constant $A$ (unlike the constants $B$ and $C$) is assumed to depend linearly on temperature $T$, and is usually written $A(T) = A_0(T - T^*)$, where $A_0$ is another material-dependent constant, and $T^*$ is the supercooling temperature of the isotropic phase. In general, all the phenomenological coefficients of the Landau–de Gennes free-energy functional depend on temperature; however, it is usually assumed that this dependence is weak (except for the $A$ term, which controls the nematic-isotropic phase transition). Additionally, including temperature-dependent elastic constants is not expected to change the reported results qualitatively.

We describe homeotropic anchoring of the director at the colloidal surfaces by the following surface anchoring free energy,

$$F_{\text{Anch}} = W \int_{\partial V} \left( Q_{ij} - Q_{ij}^s \right)^2 dS, \qquad (2)$$

where $W > 0$ is the surface anchoring strength parameter, $Q_{ij}^s = \frac{Q^s}{2}(3\nu_i\nu_j - \delta_{ij})$ with $\delta_{ij}$ being the Kronecker delta symbol, $\nu$ is the unit outward normal vector to the confining surface, and $Q^s$ is the preferred surface scalar order parameter. We defined the surface extrapolation length $\zeta = K/W$, where $K$ is an average Frank elastic constant (see below for the relations between $L_1$, $L_2$ and $K_{11}$, $K_{22}$, $K_{33}$).

The total free energy $F = F_{\text{LdG}} + F_{\text{Anch}}$ is then minimized numerically by employing the adaptive mesh finite elements method as described in more detail in Ref. [3]. We assume $V = \{-L/2 \leqslant y \leqslant L/2, -h/2 \leqslant x, z \leqslant h/2\}$, and use a uniaxial twisted nematic as the initial conditions $Q_{ij}^0$ for the minimization, i.e., $Q_{ij}^0(x) = \frac{Q^0}{2}(3n_i^0 n_j^0 - \delta_{ij})$ with $(n_x^0, n_y^0, n_z^0) = [0, \cos(\pi x/h), \sin(\pi x/h)]$. At this point we would like to emphasize that in the cholesteric phase the order parameter $Q$ is necessarily biaxial [42]. Regarding the boundary conditions at the simulation box, we set "free" boundary conditions on surfaces $y = \pm L/2$; on surfaces $x = \pm h/2$ and $z = h/2$ we use rigid boundary conditions with $n_z = 1$ and with the surface scalar order parameter which equals $Q^0$. Finally, on boundary $z = -h/2$ we fix the tensor order parameter to be equal to $Q_{ij}^0(x)$.

Following [3,42] we introduce the dimensionless temperature $\tau \equiv 24A(T)C/B^2$. The cholesteric phase is stable for $\tau < \tau_{CI}$, where the cholesteric-isotropic coexistence temperature is given by [40]

$$\tau_{CI} = \begin{cases} \frac{1}{2}\{1 + (q_0\xi)^2 + [1 + \frac{1}{3}(q_0\xi)^2]^{\frac{3}{2}}\}, & q_0\xi \leqslant 3 \\ (q_0\xi)^2, & q_0\xi > 3 \end{cases}. \qquad (3)$$

We use the following values of the bulk parameters $A_0 = 0.044 \times 10^6$ J/m³, $B = 0.816 \times 10^6$ J/m³, $C = 0.45 \times 10^6$ J/m³, $L_1 = 6 \times 10^{-12}$ J/m, $L_2 = 12 \times 10^{-12}$ J/m, and $T^* = 307$ K. The size of the computation box was set to $h \times L \times h = 1 \times 4 \times 1$ μm³, and the cholesteric pitch $P = 0.5$ μm. The size of colloidal particles, i.e., the diameter of a sphere, the side length of a cubic particle, the lateral dimension of a square platelet, or the shorter
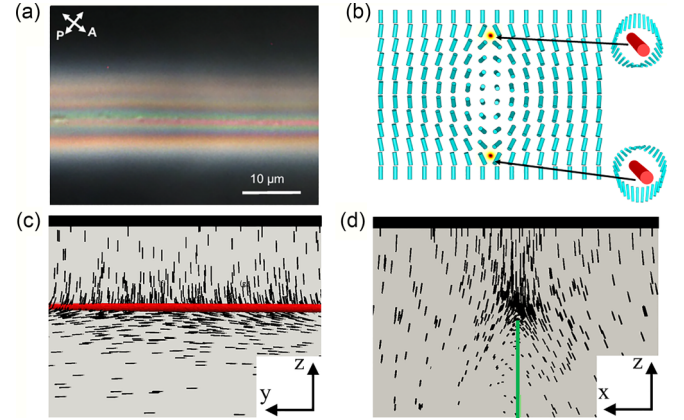


FIG. 1. (a) Polarized optical micrographs of a topological line defect decorating a cholesteric finger. (b) Director configuration in the vertical cross section of the cholesteric finger with two twist line defects, highlighted by red. The depicted structure is invariant along the normal to the cross section. The two right panels illustrate schematically the configurations of the director field (blue rods) around the defect lines at the top and bottom of the cross section. (c), (d) Director configurations (shown by black rods) around a twist disclination line as obtained by numerical minimization of the Landau–de Gennes free energy. The red tube in (c) encloses the region of a reduced nematic scalar order parameter $Q \leqslant 0.25$. The configuration (c) is taken in the $x = 0$ plane, where the center of the defect core is located. The cross-sectional configuration depicted in (d) is taken in the $y = 0$ plane which is perpendicular to the line defect. This configuration is translationally invariant along the defect line. Black bars at the top of (c), (d) schematically illustrate the confining surfaces which impose rigid homeotropic boundary conditions on the nematic director. The green line in (d) indicates the location of the twist wall.

dimension of a spherocylinder, was set to 100 nm. The spatial extension of inhomogeneous regions and the cores of topological defects is of the order of the nematic coherence length $\xi \propto A(T)^{-1/2}$ [40], which reaches its maximum $\xi = 2\sqrt{2C(3L_1 + 2L_2)/B^2} \simeq 15$ nm at the nematic-isotropic ($q_0 = 0$) transition [41].

For simplicity we set both $Q_s$ and $Q^0$ equal to the value of the scalar order parameter in the bulk nematic phase $Q_N = B(1 + \sqrt{1 - \frac{8\tau}{9}})/8C$. The following expressions relate $L_1$, $L_2$ with the Frank elastic constants: $K_{11} = K_{33} = 9Q_N^2(L_1 + L_2/2)/2$, $K_{22} = 9Q_N^2 L_1/2$.

## III. RESULTS

### A. Trapping of a spherical particle by a twist disclination line

As the first step we consider a particle-free system and obtain free-energy minimizing liquid crystal configurations bearing twist disclination lines. A typical example of the resulting configuration is shown in Figs. 1(c) and 1(d), using cross-sectional representation of the director field (black rods). The long red tube in Fig. 1(c) enclosed the region of the reduced scalar order parameter; i.e., it encloses the core of the defect line. There are two disclination lines located close to the homeotropic confining surfaces, and the whole structure is translationally invariant along the disclination
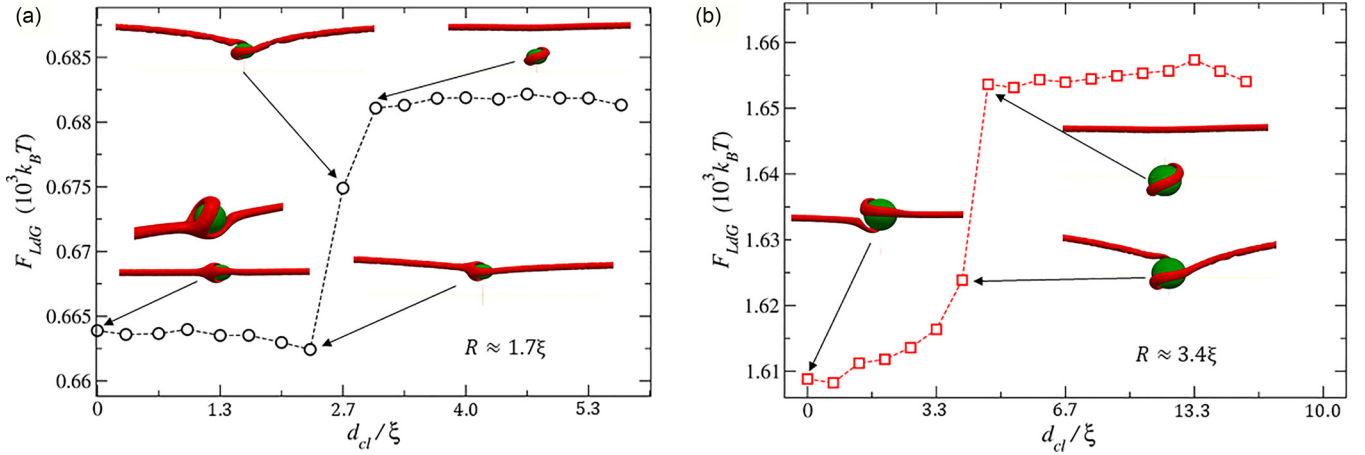
FIG. 2. Elastic entrapment of colloidal particles within the cores of twist disclination lines. Numerically calculated Landau–de Gennes free energy as a function of the separation $d_{cl}$ between the colloidal particle and the core of the disclination line obtained at two values of the radius $R$ of the colloidal particle: (a) $R \approx 1.7\xi$; (b) $R \approx 3.4\xi$, where $\xi$ is the nematic coherence length defined in Sec. II B. Insets show configurations of the colloidal particle (green spheres) at the disclination lines (red tubes enclosing the regions of the reduced nematic scalar order parameter $Q \leqslant 0.25$). The configurations correspond to data points indicated by black arrows. The results are obtained at the values of the model parameters specified in Sec. II B.

lines. Figure 1(b) shows the full cross-sectional view of this structure, known as a cholesteric finger CF-3 (of one of several different types of the cholesteric fingers) [42–44], which is composed of a $180°$-twist wall and two twist disclinations lines, whose cores are highlighted in red at the bottom and the top confining surface. Polarized optical micrographs of one such topological defect line decorating the cholesteric finger is shown in Fig. 1(a). The distance from the line to the confining cell surface depends on the ratio of the cholesteric pitch and the separation $L_z$ between the homeotropic surfaces. The nonsingular twist wall is a one-dimensional (1D) soliton which is energetically favorable due to the LC chirality and imbedded into a uniform nematic background $n_0$ with the help of the defect lines.

Within the solitonic LC twist wall, $\mathbf{n}(\mathbf{r})$ has no component perpendicular to the wall; i.e., the director is effectively confined to a 2D plane and the corresponding effective order-parameter space is the real projective line $RP^1$ [43]. Director rotation by $180°$ across the LC twist wall covers the $RP^1$ exactly once enabling a smooth embedding of the 1D twisted structure into the uniform far-field director background. CF-3 provides an example of the coexistence of nonsingular and singular topological defects which enables continuous embedding of the 1D solitonic director configuration into a finite 3D slit geometry with homeotropic anchoring at the confining surfaces. In all subsequent numerical calculations with colloidal particles included, we use LC configurations like the one shown in Fig. 1 to construct initial LC configurations.

Figure 2 demonstrates how a twist disclination line can be used to entrap spherical colloidal particles, where we plot the Landau–de Gennes free energy $F_{LdG}$ as a function of the particle-line separation. We initiate the minimization of the functional given in Eq. (1) augmented with the surface free energy, Eq. (2), by using the pregenerated cholesteric finger LC configurations with an embedded colloidal particle at a given initial distance $d_{cl}$ to the defect line. The high-energy part of $F_{LdG}(d_{cl})$ curves at large $d_{cl}$ corresponds to discon-

nected particle-line configurations. Below a certain threshold separation, the line can entrap the particle by strongly deviating from its linear shape; see inset configurations in Fig. 2(a) at $d_{cl}/\xi \approx 2.7$ and in Fig. 2(b) at $d_{cl}/\xi \approx 4.1$ Despite this line deformation the net free energy gets significantly reduced and upon further decrease of $d_{cl}$ reaches the global minimum at $d_{cl} \approx 0$. At these sizes ($\sim 100$ nm) of the colloidal particle, the free-energy difference between the detached and fully entrapped configurations is of the order of $100 k_B T$; i.e., the particles get irreversibly trapped within the twist disclination's defect core.

### B. Colloidal spheres and cubes trapped by the disclination line

Here we describe behavior of effective interactions between pairs of line-entrapped colloidal spheres and cubes, focusing on the effect of temperature. Here and in all the subsequent sections we assume homeotropic anchoring given by Eq. (2) at the surfaces of the colloidal particles. Initial conditions are constructed by using the precalculated colloid-free LC configurations, into which we insert "by hand" two colloidal particles. The positions of the particles relative to the defect line correspond to the global minimum of the single particle $F_{LdG}(d_{cl})$, see Fig. 2 for an example, and are kept constant in the course of the minimization; only the particle positions along the defect line are varied. Figures 3(a) and 3(b) show $F_{LdG}$ as a function of the colloid-colloid separation $d_{cc}$ for spheres, panel (a), and cubes, panel (b), at several different values of temperature (proportional to parameter $A$ in Eq. (1); recall that at the nematic-isotropic coexistence $A_{NI} \simeq 0.062$). Surprisingly, colloidal cubes exhibit attractive interactions at all values of temperature, and the interaction strength depends weakly on the value of $A$. In contrast, colloidal spheres repel each other at low temperatures (small values of $A$), with strongly temperature-dependent repulsion strength [see black, blue, and magenta symbols and curves in Fig. 3(a)]. We also find that at some threshold value $A = A^{th}$, where $0.05 < A^{th} <$
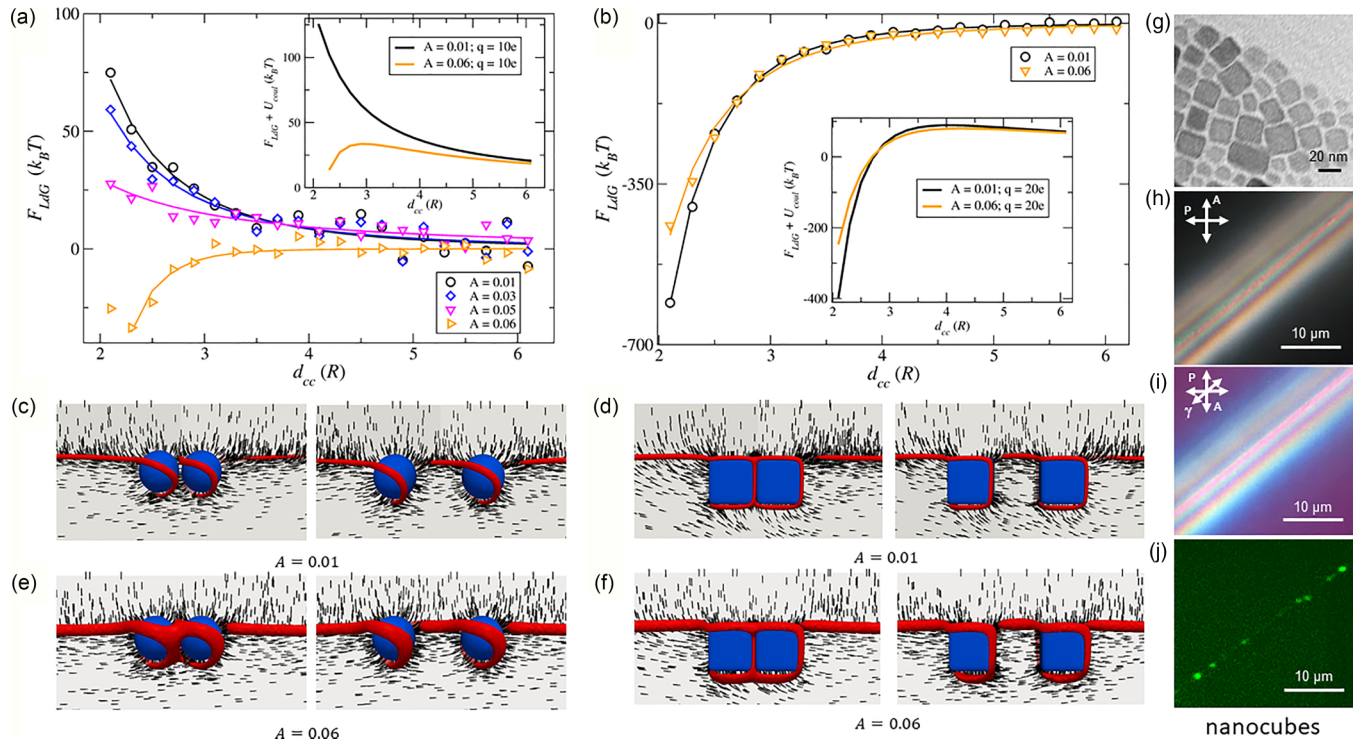
FIG. 3. Effective interactions between pairs of colloidal spheres and cubes entrapped within the core of the twist disclination lines. Landau–de Gennes free energy $F_{LdG}$ [see Eq. (1) in Sec. II B] as a function of the center-to-center distance $d_{cc}$ between two spherical (a) and cubic (b) particles. Different symbols and fitting curves correspond to different values of temperature quantified by parameter $A$; see Eq. (1) in Sec. II B. Symbols in (a), (b) represent numerically calculated values; solid curves are guides to the eye. In both cases a finite homeotropic anchoring is assumed at the surfaces of the particles, characterized by the surface extrapolation length $K/W \approx 10^{-3}$ µm. The radius of the spheres, and the side length of the cubes $R \approx 3.4\xi$. Insets in (a), (b) show superimposed $F_{LdG}$ and Coulomb repulsive potential assuming that each of the colloids carries an electrostatic charge of $10e$ (a), and $20e$ (b), where $e$ is the elementary charge. (c)–(f) Cross-sectional representation of the nematic director (black rods) around the colloidal particles (depicted by blue surfaces) at two selected separations between the colloids and at low (c), (d), and high (e), (f) values of temperature. Red tubes enclose the regions of the reduced nematic scalar order parameter $Q \leqslant 0.25$ at $A = 0.01$, and $Q \leqslant 0.2$ at $A = 0.06$. (g) Transmission electron microscope (TEM) micrographs of nanocubes (size $\approx 20$ nm) deposited onto a copper grid. (h), (i) Polarized optical micrographs of a cholesteric finger with line defect and with nanocubes trapped in the singular defect core without (h) and with (i) a retardation plate. (j) Luminescence based confocal microscopy images of the nanocubes in the line defect.

0.06 the reversal of the direction of the interaction force takes place, and the force becomes attractive for $A > A^{th}$ [see the orange symbols and the curve in Fig. 3(a)]. The origin of this high-temperature attraction at small $d_{cc}$ can be qualitatively understood by inspecting the evolution, with varying $d_{cc}$, of the defect line arrangement around the particles depicted in Fig. 3(e). The first observation is that the core of the defect line is significantly bulkier at high temperatures as compared to its low-temperature counterpart, comparing the diameters of the red tubes in Fig. 3(c) with that in Fig. 3(e). Now at large particle separations $d_{cc} \geqslant 3R$ [see the configuration in the right panel in Fig. 3(e)], the geometric configuration of the line core is topologically trivial; i.e., it features just bending deformation while going around the colloidal particles. It is not so for $d_{cc} < 3$, when we observe two tilted closed loops encircling the colloidal particles; see left panel in Fig. 3(e). This topological reconfiguration of the defect line at short distances gives rise to a crossover from the large distance ($d_{cc} \geqslant 3R$) weak repulsion to the short distance attraction. In some sense this behavior is similar to a bridging attraction which emerges between colloidal particles in a simple fluid, when a liquid phase condenses between the particles at the

distance below a threshold, while outside there is a vapor phase [45–48]. The formation of this liquid bridge leads to a strong colloidal attraction [46]. In our case, the role of such a bridge is played by a defect core "phase" (with the reduced orientational ordering of the LC), which condenses between the spheres, see the corresponding region in the left panel in Fig. 3(e), where the two aforementioned defect loops merge to form in between the particles a region of the reduced scalar order parameter. We would like to emphasize that the bridge responsible for the sphere attraction is formed by a nematic phase with the reduced orientational order. Importantly, the extension of the regions around the spheres where the nematic order is decreased increases with the increase of temperature. This bridging effect is operational for temperatures very close to the nematic-isotropic phase coexistence. For lower temperatures, the repulsion due to the surface anchoring is observed.

Additional contributions are expected to the effective nanoparticle's interactions at short separations of the order of the nematic coherence length $\xi \sim 15$ nm, which are due to the gradients in the scalar order parameter. The resulting forces are relatively weak as compared to the elastic forces
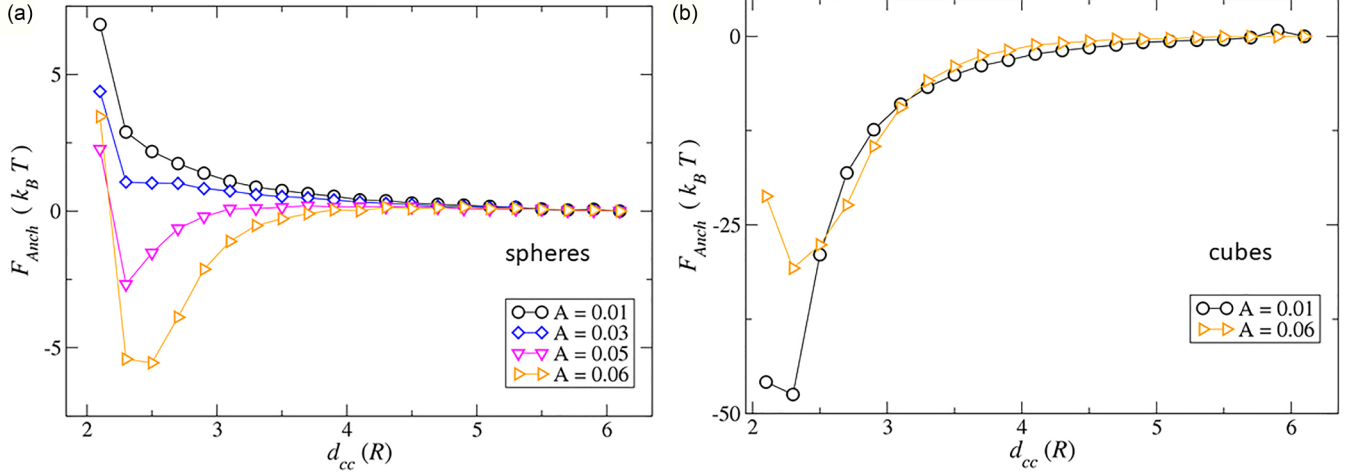
FIG. 4. Numerically calculated surface anchoring free energy $F_{\text{Anch}}$ [see Eq. (2) in Sec. II B] as a function of the center-to-center distance $d_{\text{cc}}$ between two spherical (a) and cubic (b) colloidal particles. Different symbols correspond to different values of temperature as given by parameter $A$; see Eq. (1) in Sec. II B. The particle homeotropic anchoring is characterized by the surface extrapolation length $K/W \approx 10^{-3}$ μm.

due to the gradients of the nematic director and will be addressed elsewhere with more powerful experimental tools and an advanced numerical method.

The monotonous repulsive interaction between the spheres, observed at lower temperatures, can be interpreted in terms of the nematostatic formalism [14] and associated elastic multipoles.

The basic idea is related to the fact that far from a colloidal particle the director field $n(r) \approx n_0 + \delta n$, where the correction to the far-field director term $\delta n$ is small and $(n_0 \cdot \delta n) = 0$ holds. Additionally, the components of $\delta n$ obeys the Laplace equation whose solution can be presented in a form of a multipole expansion. This idea was employed to demonstrate a monopolelike attraction between micron-sized colloidal particles in nematic LC with a nonuniform background director field [33].

Thus, the LC structure around the spheres is consistent with the leading elastic quadrupole contribution. The resulting like quadrupoles repulsion is consistent with the behavior shown in Fig. 3(a). The repulsion strength is controlled by the temperature-dependent elastic quadrupole moment. Surprisingly, the defect line plays a minor role in this temperature range, in contrast to the case of high-aspect-ratio spherocylinders as we discuss below. In the case of the cubes, shown in Figs. 3(b), 3(d), and 3(f), the strong attraction can be understood as induced by two like elastic monopoles, and the symmetry of the director configurations around the two cubes [Fig. 3(d)] is consistent with that due to elastic monopoles. The strength of the attraction is controllable by temperature by modifying the elastic multipole moments. The theoretically predicted attraction between nanocubes is confirmed indirectly by experimental observations, reported in Figs. 3(g)–3(j). Indeed, the bright luminescence spots clearly visible in Fig. 3(j) originate from compact aggregates of nanocubes, as isolated particles cannot produce such bright patterns according to our observations within the same liquid crystal outside of the defect lines. Additionally, the particles inside the line defects show different brightness, due to varying aggregation levels, whereas

minimal intensity variation is expected between single particles.

Figure 4 reports the behavior of the surface anchoring free energy $F_{\text{Anch}}$ as a function of the separation between two homeotropic spheres [Fig. 4(a)] and homeotropic cubes [Fig. 4(b)]. In this case of relatively large values of the anchoring strength, with the surface extrapolation length $K/W \approx 10^{-3}$ μm, the contribution of the surface free energy is an order of magnitude smaller compared to the bulk term $F_{LdG}$. It is easy to understand why $F_{\text{Anch}}$ decreases in the case of cubes at all temperatures. This behavior is driven by the parallel geometry of the closest faces of two interacting cubes; the closer these faces are, the easier it is to satisfy the preferred homeotropic director alignment. This is not the case for spheres: Upon approaching, the neighboring boundaries frustrate the aligning preference of each other, and this gives rise to the repulsive $F_{\text{Anch}}$; see the black circles and blue diamonds in Fig. 4(a). Surprisingly, by increasing the temperature $F_{Anch}$ becomes attractive; see magenta and orange triangles in Fig. 4(a). One of the reasons, as $F_{\text{Anch}} \propto Q_0^2$, is the reduction of the scalar order parameter in the region between the particles upon reducing $d_{\text{cc}}$, due to the above-mentioned formation of the defect core phase at small particle separations.

Next, we discuss the case of weaker homeotropic anchoring, characterized by the surface extrapolation length $K/W \approx 2 \times 10^{-2}$ μm, with the corresponding results for both $F_{\text{LdG}}(d_{\text{cc}})$ and $F_{\text{Anch}}(d_{\text{cc}})$ depicted in Fig. 5. Now, both terms of the total interaction are of the same order of magnitude. The main differences as compared to the strong anchoring case in Fig. 3 are reflected in the Landau–de Gennes free energy, which now reveals a repulsive nature for all cases studied. The director configurations around cubes, Figs. 5(g) and 5(h), is consistent in this case with the quadrupolar symmetry resulting in a repulsive interaction between like quadrupoles. Additionally, the cores of the defect do not extend far from the colloidal surfaces into the LC domain, like in the case of larger $W$, but are hidden (virtually) within the particles. This turns off the bridging mechanism [see the left panel in Fig. 5(f)] responsible for the short distance attraction between
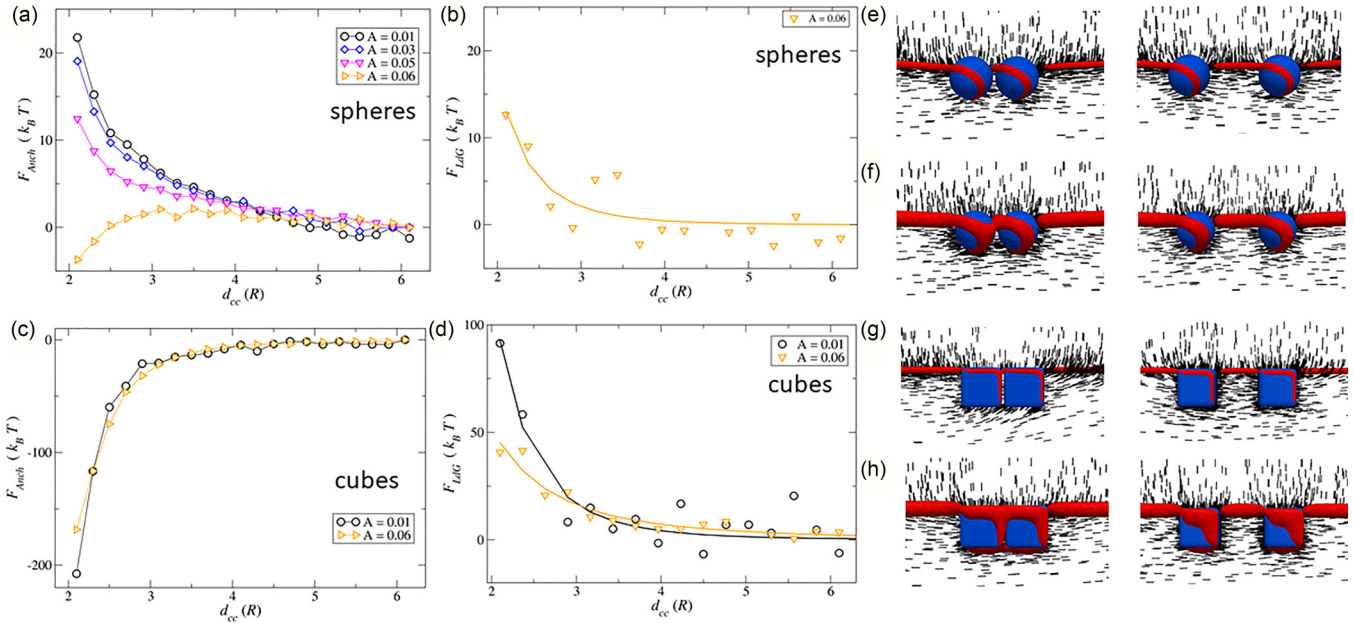
FIG. 5. Numerically calculated Landau–de Gennes free energy $F_{LdG}$ (b), (d), and surface anchoring free energy $F_{Anch}$ (a), (c) as functions of the center-to-center distance $d_{cc}$ between two spherical (a), (b) and cubic (c), (d) colloidal particles. Different symbols correspond to different values of temperature as given by parameter $A$; see Eq. (1) in Sec. II B. The particle homeotropic anchoring is characterized by the surface extrapolation length $K/W \approx 2 \times 10^{-2}$ μm. The radius of the spheres, and the side length of the cubes $R \approx 3.4\xi$. (e)–(h) Cross-sectional representation of the nematic director (black rods) around the colloidal particles (blue surfaces) at two selected separations between the colloids and at low (e), (g), and high (f), (h) values of temperature. Red tubes enclose the regions of the reduced nematic scalar order parameter, $Q \leqslant 0.25$ at $A = 0.01$, and $Q \leqslant 0.2$ at $A = 0.06$.

spheres at high temperatures in the previous case. Now, no defect core matter condenses between the spheres, and they always repel each other [see Fig. 5(b)]. The anchoring free energy, Figs. 5(a) and 5(c), exhibits qualitatively similar behavior as in the case of Fig. 4, beside the absence of very strong repulsion at short distances. The combined interaction potential between cubes, as given by the sum $F_{LdG} + F_{Anch}$, is, however, attractive because it is dominated by a much stronger attractive $F_{Anch}$, Fig. 5(c). In the case of the spheres at the highest temperature, $A = 0.06$, the repulsive $F_{LdG}$ dominates over $F_{Anch}$ [compare data shown with orange triangles in Figs. 5(b) and 5(c)].

### C. Rodlike particles

Our next goal is to reveal the behavior of colloidal nanorods under the confinement of twist disclinations. Figures 6(j)–6(l) demonstrate optical micrographs of gold nanorods with thin silica shells [see Fig. 6(g)] entrapped in the core of twist disclinations. We observe that in this specific system the rodlike core-shell nanoparticles align parallel to the disclination core, and experience long repulsion at distances more than an order of magnitude larger than the particle dimensions, Figs. 6(h) and 6(i). In experiments, the nanoparticles can be moved along the defect line by using infrared laser tweezers and can be optically manipulated. This capability is a key to understanding properties of nanoparticles and interactions between them at a single particle level or at the level of a few nanoparticles. The interaction potential between two entrapped nanorods, shown in Fig. 6(i), was probed when the rods were brought close to each other using optical tweezers and then released. The corresponding variation of the particle

separation with time when the optical traps are switched off, demonstrating the repulsion between the nanorods, is reported in Fig. 6(h). In a qualitative agreement, with the theoretical predictions in Fig. 6(a), the repulsion strength can be increased by reducing the temperature of the LC host, as seen by comparing plots based on measurements at room temperature and at $45\,^{\circ}$C. In experiments, we did not observe a crossover from a repulsive to attractive behavior above some threshold temperature, as is predicted theoretically; see data shown by orange triangles in Fig. 6(a). One of the reasons could be the presence of electrostatic charges on nanorods leading to an overall repulsive behavior, as shown in the inset of Fig. 6(a). Still another reason could be related to the difference between the values of the surface extrapolation length in the experimental, $\approx 0.1$ μm, and the model, $\approx 0.001$ μm, systems. Still, the experiments and theory show a similar trend of weakening interactions with increasing temperature.

Numerical calculations also reveal strong shape dependence of the effective interactions between the rods, Figs. 6(a), 6(b), 7(a), and 7(b). While for rods with a small aspect ratio we observe similar dependence on temperature as the one reported in Fig. 3(a) for spherical particles, surprisingly, by increasing the aspect ratio, we can achieve attraction at all temperatures considered; see Figs. 6(b), 7(a), and 7(b). This finding is supported by experimental results in Fig. 7(g) which shows assemblies of high-aspect-ratio nanorods in the defect core. Our qualitative explanation of this aspect ratio induced crossover to attractive behavior is that (i) the strength of the elastic quadrupolar moment decreases with the particle elongation; (ii) high-aspect-ratio rods generate in their vicinity a large excess of energetically unfavorable defect core
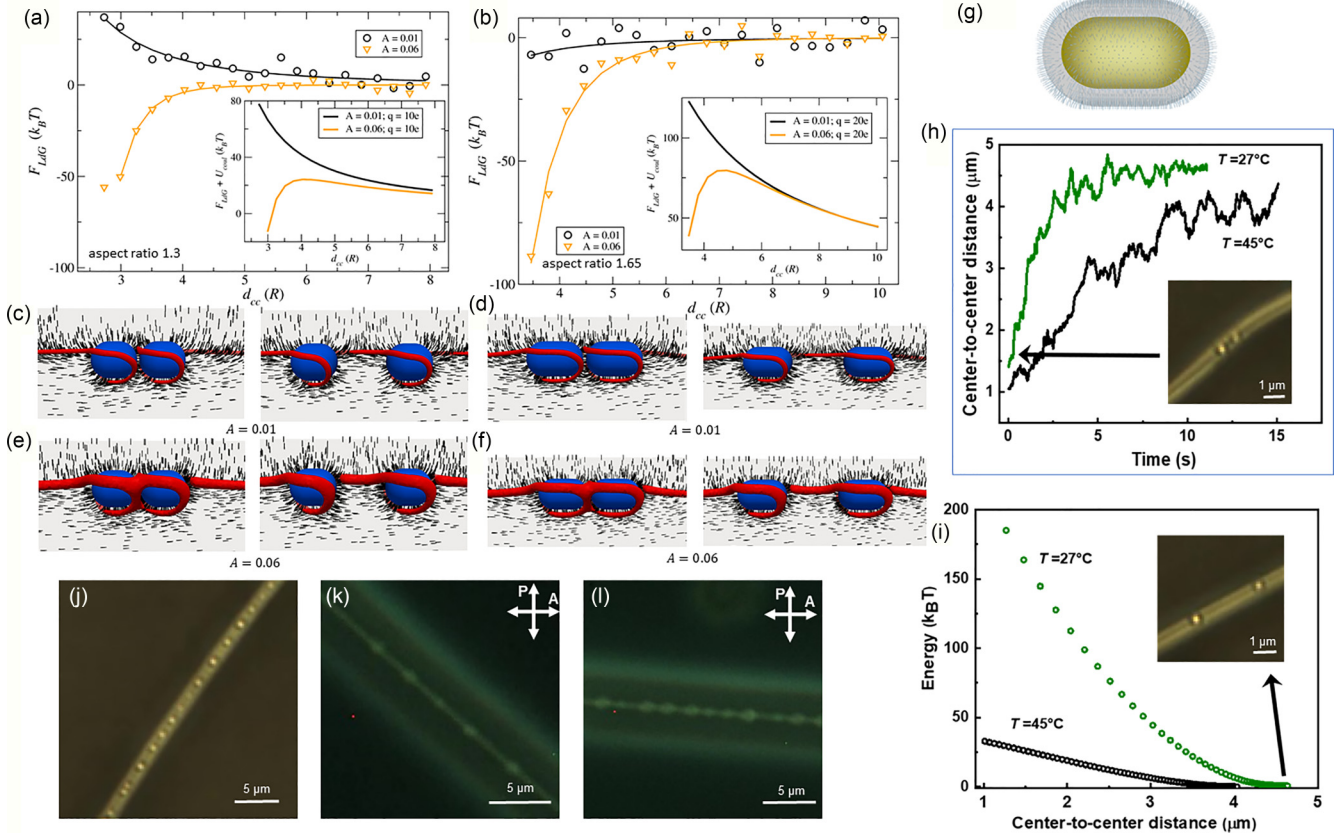
FIG. 6. Effective interactions between pairs of spherocylinders entrapped within the core of the twist disclination lines. Landau–de Gennes free energy $F_{LdG}$ [see Eq. (1) in Sec. II B] as a function of the center-to-center distance $d_{cc}$ between two spherocyliners with the aspect ratio $\kappa = 1.3$ (a) and $\kappa = 1.65$ (b), the radius of the spherical caps, and the central cylindrical parts $R \approx 3.4\xi$. Different symbols and fitting curves correspond to different values of temperature as given by parameter $A$; see Eq. (1) in Sec. II B. Symbols in (a), (b) represent numerically calculated values; solid curves are guides to the eye. In both cases a finite homeotropic anchoring is assumed at the surfaces of the particles, characterized by the surface extrapolation length $K/W \approx 10^{-3}$ µm. Insets in (a), (b) show superimposed $F_{LdG}$ and Coulomb repulsive potential assuming that each of the particles carries an electrostatic charge of $10e$ (a), and $20e$ (b), where $e$ is the elementary charge. (c)–(f) Cross-sectional representation of the nematic director (black rods) around the colloidal particles (blue surfaces) at two selected separations between the colloids and at low (c), (d), and high (e), (f) values of temperature. Red tubes enclose the regions of the reduced nematic scalar order parameter $Q \leqslant 0.25$ at $A = 0.01$, and $Q \leqslant 0.2$ at $A = 0.06$. (g) Schematics of the GNR showing the silica shell and DMOAP surfactant monolayer; real GNRs have the size $\approx 40 \times 60$ nm. (h) Variation of center-to-center spacing with time when two GNRs were moved close to each other with the help of an optical tweezer and then released, demonstrating repulsion between the nanoparticles at $T = 27\,^\circ\mathrm{C}$ and $45\,^\circ\mathrm{C}$. Inset shows the dark-field optical micrograph of two GNRs separated by $\sim 1$ µm inside the line defect when they are moved close to each other with the help of an optical tweezer. (i) Interaction potential between two GNRs at $T = 27\,^\circ\mathrm{C}$ and $45\,^\circ\mathrm{C}$ calculated based on the curves in (h). Inset shows the dark-field optical micrographs of two GNRs trapped inside a line defect after releasing the particles from the optical traps. (j) Dark-field optical micrograph, showing the assemblies of individual GNRs inside line defects. (k), (l) Polarized optical micrographs of the assemblies of individual GNRs inside the line defect.

matter, as is shown in Figs. 7(c) and 7(d) by the long multiple defect loops around the rods. The system seemingly can minimize this energy cost due to the defect length at shorter rod separation, resulting in an overall attractive behavior. Experimentally we also found that highly charged high-aspect-ratio colloidal rods can be prevented from irreversible binding within the defects due to electrostatic repulsions.

### D. Platelets

Next, we focus on a plateletlike geometry of colloidal inclusions (Fig. 8). Here we discuss effective interactions between thin platelets [see Fig. 8(i)] entrapped by the defect line. In this case we fix the relative particle orientation in face-

to-face [Fig. 8(e)] or edge-to-edge [Fig. 8(g)] configurations. $F_{LdG}$ as a function of particle separation is shown in Figs. 8(a) and 8(b) for the face-to-face and edge-to-edge configurations, respectively. In both cases we find strong attraction, similarly to the case of the cubic particles in Fig. 3(b). In both cases we attribute the attractive behavior to the leading monopolelike distortions of the LC director, with the monopole moments of equal signs. This conclusion is supported by a visual inspection of the LC director configurations, depicted in Figs. 8(e)–8(h). The anchoring free energy, Figs. 8(c) and 8(d), also exhibits an attractive trend in both cases, but with the interaction strength which is 5–10 times weaker compared to $F_{LdG}$ term. This strong attractive behavior of the nanoplates is in qualitative agreement with the experimental observations
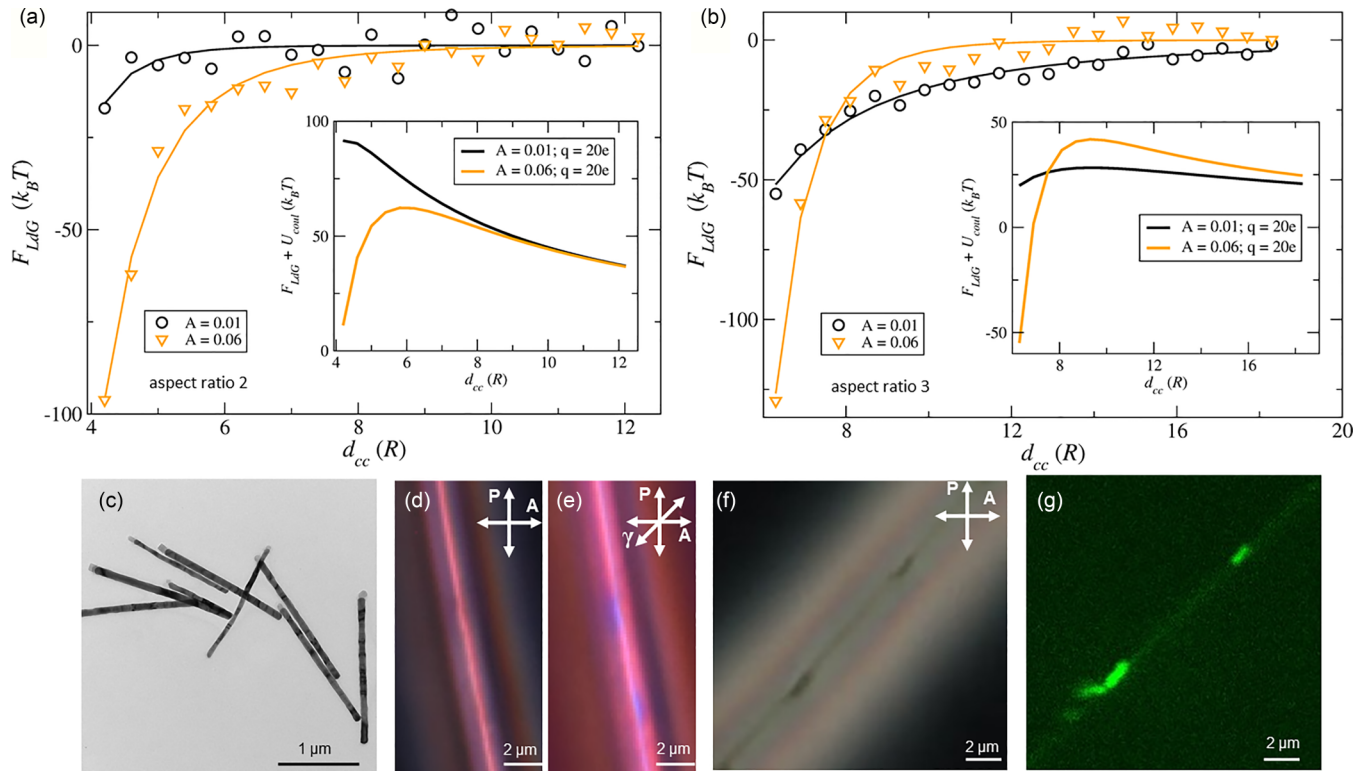
FIG. 7. Effective interactions between pairs of spherocylinders entrapped within the core of the twist disclination lines. Landau–de Gennes free energy $F_{LdG}$ as a function of the center-to-center distance $d_{cc}$ between two spherocyliners with the aspect ratio $\kappa = 2$ (a) and $\kappa = 3$ (b), the radius of the spherical caps, and the central cylindrical parts $R \approx 3.4\xi$. Different symbols and fitting curves correspond to different values of temperature as given by parameter $A$; see Eq. (1) in Sec. II B. Symbols in (a), (b) represent numerically calculated values; solid curves are guides to the eye. In both cases a finite homeotropic anchoring is assumed at the surfaces of the particles, characterized by the surface extrapolation length $K/W \approx 10^{-3}$ μm. Insets in (a), (b) show superimposed $F_{LdG}$ and Coulomb repulsive potential assuming that each of the particles carries an electrostatic charge of $20e$, where $e$ is the elementary charge. (c) TEM micrograph of upconversion nanorods (20 nm × 1.6 μm) deposited on a copper grid. (d)–(f) Polarized optical micrographs of upconversion nanorods trapped inside line defects without (d), (f), and with (e) a retardation plate. (g) Luminescence based confocal microscopy image of upconversion nanorods trapped inside the line defect.

in Figs. 8(j)–8(l), where we clearly identified bright spots on the confocal fluorescence microscopy image of nanoplates inside the line defect, Fig. 8(j). Individual nanoplates are too small to produce such bright fluorescent spots, which may only result from aggregates of many nanoplates. However, we cannot tell whether the nanoplates have assembled face-to-face, or edge-to-edge, but numerical analysis predicts the face-to-face assembly to be the more stable one.

By reducing the anchoring strength, we find a repulsive character of the $F_{LdG}(d_{cc})$ curve, as shown in Fig. 9(b), for the edge-to-edge platelet arrangement. This behavior is similar to that of the cubes with weak anchoring shown in Fig. 5(d). LC director configuration in Fig. 9(d) is consistent with the superposition of two dissimilar elastic monopoles which are expected to interact repulsively [13,14,32]. In contrast, $F_{Anch}(d_{cc})$ depicted in Fig. 9(a) favors the attraction of the platelets and this attraction is much stronger compared to the repulsion driven by the bulk free energy $F_{LdG}$, such that the total interaction has an attractive character.

## IV. DISCUSSION AND CONCLUSIONS

Here we exploited twist disclination lines to confine the position of colloidal particles along the line contour and to

systematically investigate the effective interparticle interaction as a function of the particle shape, temperature, and the strength of homeotropic boundary conditions. Regarding the latter, we have considered the regime of the strong boundary conditions, with the ratio of the particle size to the surface extrapolation length $R/\zeta \approx 50$, and the regime of weak surface anchoring with $R/\zeta \approx 2.5$. In the last case the boundary conditions can be violated, and the corresponding surface free energy $F_{Anch}$ dominates over the bulk contribution quantified by $F_{LdG}$. In this case regions of the reduced scalar order parameter can also appear near locations of nanoparticles that have a local easy axis direction not matching with the far-field director $n_0$.

The spherical particles with strong surface anchoring repel each other at low temperatures, with temperature-dependent interaction strength. The director distortions around the particles are consistent with elastic quadrupoles, and the strength of the quadrupole moment decreases with the increase of temperature. Above a certain threshold temperature we observe short-range attraction driven by merging of the regions of reduced scalar order parameters—a phenomenon reminiscent of the bridging effect when liquid bridges condense between colloidal particles in simple fluids. For weak anchoring we did not find this overlap of the defect core matter and $F_{LdG}$
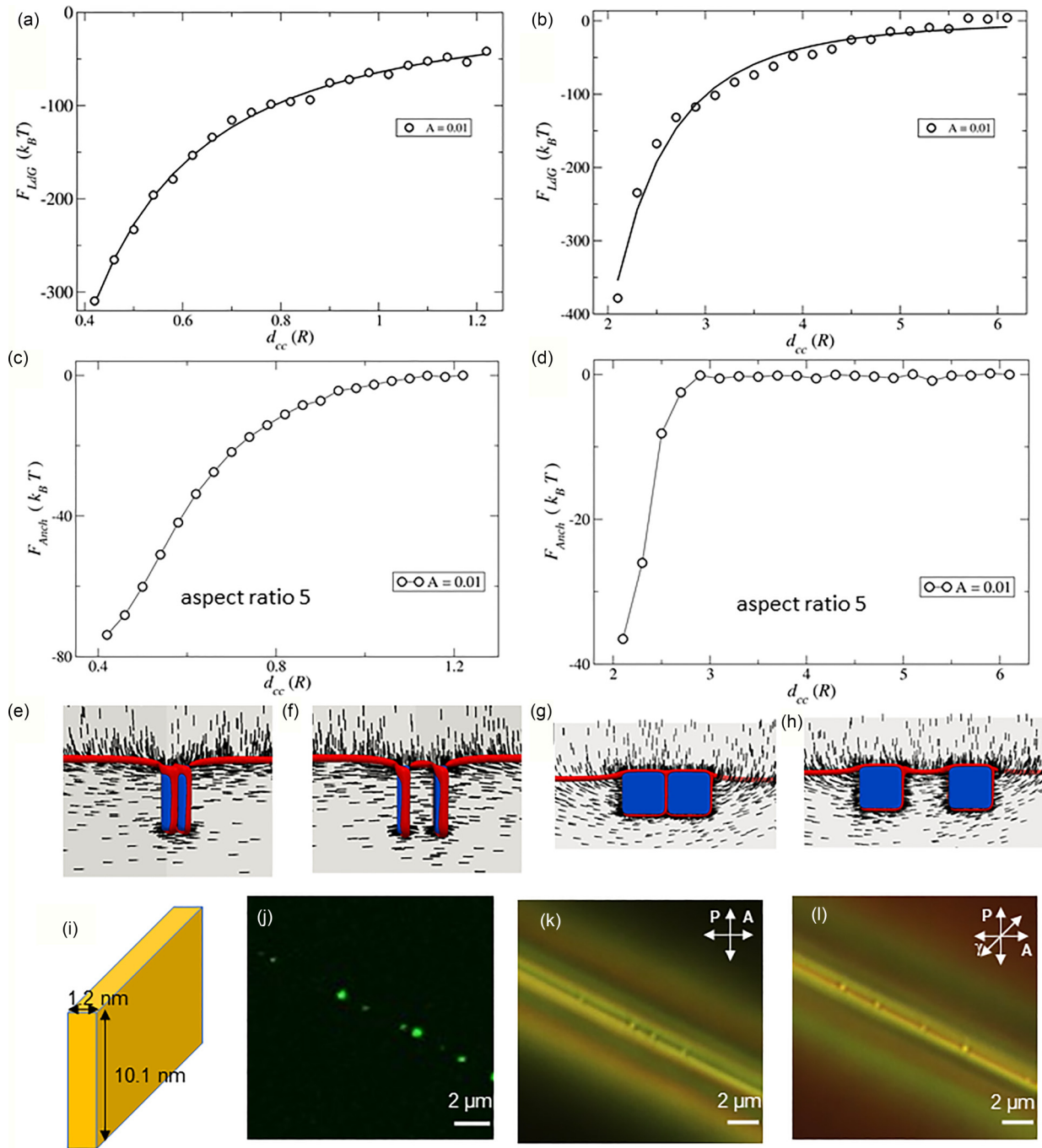
FIG. 8. Effective interactions between pairs of colloidal platelets entrapped within the core of the twist disclination lines. Landau–de Gennes free energy $F_{LdG}$ as a function of the center-to-center distance $d_{cc}$ between two platelets with the aspect ratio $\kappa = 5$ and face-to-face (a), and edge-to-edge (b) orientation. The side length of the square $R \approx 3.4\xi$. Surface anchoring free energy $F_{Anch}$ obtained for face-to-face (c), and edge-to-edge (d) platelet alignment. Symbols in (a), (b) represent numerically calculated values; solid curves are guides to the eye. A finite homeotropic anchoring is assumed at the surfaces of the particles, characterized by the surface extrapolation length $K/W \approx 10^{-3}$ μm. (e)–(h) Cross-sectional representation of the nematic director (black rods) around the platelets (blue surfaces) at two selected separations between the colloids. Red tubes enclose the regions of the reduced nematic scalar order parameter $Q \leqslant 0.25$. (i) Schematic of CdSe nanoplate with dimensions marked in the illustration. (j) Confocal fluorescence microscopy image of CdSe nanoplates inside the line defect. (k), (l) polarized optical micrographs of CdSe nanoplatelets inside the line defects without (k) and with (l) retardation plate.

exhibited or facilitated repulsive behavior. Cuboid and platelet colloidal particles exhibit attraction at all values of temperatures, and anchoring strength. However, the origin of this attraction is different in the strong and the weak anchoring regimes, while in the first case, the attraction is driven by the bulk free-energy term, with the leading contribution stemming from the like elastic monopoles. In the case of the weak anchoring the attractive surface free energy $F_{Anch}$ dominated and $F_{LdG}$ was found driving repulsion consistent with the contribution from unlike elastic monopoles, i.e., with monopole
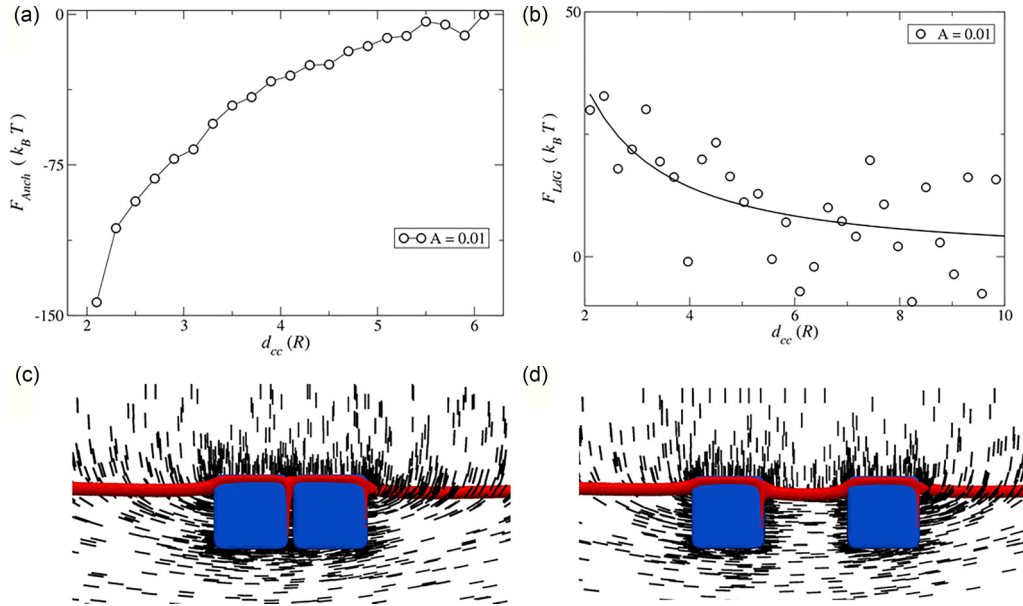
FIG. 9. Effective interactions between pairs of colloidal platelets entrapped within the core of the twist disclination lines and aligned edge to edge and with the aspect ratio $\kappa = 5$ and the side length of the square $R \approx 3.4\xi$. Landau–de Gennes free energy $F_{\mathrm{LdG}}$ (b) and the surface anchoring free energy $F_{\mathrm{Anch}}$ (a) as functions of the center-to-center distance $d_{\mathrm{cc}}$ between platelets. Symbols in (b) represent numerically calculated values; solid curves are guides to the eye. A finite homeotropic anchoring is assumed at the surfaces of the particles, characterized by the surface extrapolation length $K/W \approx 2 \times 10^{-2}$ µm. (e)–(h) Cross-sectional representation of the nematic director (black rods) around the platelets (blue surfaces) at two selected separations between the colloids. Red tubes enclose the regions of the reduced nematic scalar order parameter $Q \leqslant 0.25$.

moments of opposite signs. Rodlike colloidal particles of moderate aspect ratios behave similarly to the spherical ones, and by increasing the aspect ratio beyond a certain threshold we observed only attractive interactions. We related this to the minimization of the line energy associated with the core of the defect line.

One possible extension of this work is to consider the ultra-weak anchoring regime with $R/\zeta \ll 1$, which can be achieved by reducing either the anchoring strength or the particle size. In the last case, we expect that the nanoparticle will be completely immersed in the defect core, and its behavior will be controlled solely by the surface free energy $F_{\mathrm{Anch}}$. There exists a large variety of topologically and structurally different lines which raises the question of how different features of defect lines influence entrapment of nanoparticles and interactions between them. Another open question is related to the behavior of nanoparticles with planar or conic degenerate anchoring boundary conditions. From the application point of view various nanoparticles including gold nanorods, quantum dots, and plasmonic nanoparticles can be entrapped in defect lines and then assembled into one-dimensional crystals as well as mixed crystal with several types of nanoparticles with controlled distance between the particles.

In summary, this work described a nanoscience toolkit which exploited interactions of nanoparticles with the gradients of LC order parameter, director field, and topological defects. The diversity of reported physical behaviors depending on particle shapes and dimensions may provide a way to develop means for precise positioning of different nanoparticles with respect to each other along the topological defect lines, which could be potentially of interest for applications in nanophotonics and self-assembly based nanomanufacturing.

[1] A. Einstein, Ann. Phys. **324**, 371 (1906).
[2] V. N. Manoharan, Science **349**, 1253751 (2015).
[3] M. Tasinkevych, N. M. Silvestre, and M. M. Telo da Gama, New J. Phys. **14**, 073030 (2012).
[4] I. I. Smalyukh, Annu. Rev. Condens. Matter Phys. **9**, 207 (2018).
[5] I. Mušević, *Liquid Crystal Colloids* (Springer, Berlin, 2017).

[6] P. Poulin, H. Stark, T. C. Lubensky, and D. A. Weitz, Science **275**, 1770 (1997).

[7] C. P. Lapointe, T. G. Mason, and I. I. Smalyukh, Science **326**, 1083 (2009).

[8] A. Martinez, L. Hermosillo, M. Tasinkevych, and I. I. Smalyukh, Proc. Natl. Acad. Sci. USA **112**, 4546 (2015).

[9] Y. Yuan, A. Martinez, B. Senyuk, M. Tasinkevych, and I. I. Smalyukh, Nat. Mater. **17**, 71 (2018).

[10] S. B. Chernyshuk and B. I. Lev, Phys. Rev. E **84**, 011707 (2011).

[11] T. C. Lubensky, D. Pettey, N. Currier, and H. Stark, Phys. Rev. E **57**, 610 (1998).

[12] B. I. Lev, S. B. Chernyshuk, P. M. Tomchuk, and H. Yokoyama, Phys. Rev. E **65**, 021709 (2002).

[13] V. M. Pergamenshchik and V. A. Uzunova, Phys. Rev. E **83**, 021701 (2011).

[14] V. M. Pergamenshchik and V. A. Uzunova, Condens. Matter Phys. **13**, 1 (2010).

[15] I. Muševič, M. Škarabot, U. Tkalec, M. Ravnik, and S. Žumer, Science **313**, 954 (2006).

[16] B. Senyuk, J. Aplinc, M. Ravnik, and I. I. Smalyukh, Nat. Commun. **10**, 1 (2019).

[17] Y. Yuan, M. Tasinkevych, and I. I. Smalyukh, Nat. Commun. **11**, 188 (2020).

[18] M. Tasinkevych, N. M. Silvestre, P. Patricio, and M. M. Telo da Gama, Eur. Phys. J. E **9**, 341 (2002).

[19] A. Nych, U. Ognysta, M. Škarabot, M. Ravnik, S. Žumer, and I. Muševič, Nat. Commun. **4**, 1489 (2013).

[20] H. Mundoor, B. Senyuk, and I. I. Smalyukh, Science **352**, 69 (2016).

[21] A. Mertelj, D. Lisjak, M. Drofenik, and M. Čopič, Nature (London) **504**, 237 (2013).

[22] H. Mundoor, S. Park, B. Senyuk, H. H. Wensink, and I. I. Smalyukh, Science **360**, 768 (2018).

[23] Q. Liu, P. J. Ackerman, T. C. Lubensky, and I. I. Smalyukh, Proc. Natl Acad. Sci. USA **113**, 10479 (2016).

[24] H. Mundoor, J.-S. Wu, H. H. Wensink, and I. I. Smalyukh, Nature (London) **590**, 268 (2021).

[25] X. Wang, D. S. Miller, E. Bukusoglu, J. J. de Pablo, and N. L. Abbott, Nat. Mater. **15**, 106 (2016).

[26] B. Fleury, B. Senyuk, M. Tasinkevych, and I. I. Smalyukh, Nano Lett. **20**, 7835 (2020).

[27] B. Senyuk, J. S. Evans, P. J. Ackerman, T. Lee, P. Manna, L. Vigderman, E. R. Zubarev, J. van de Lagemaat, and I. I. Smalyukh, Nano. Lett. **12**, 955 (2012).

[28] M. Zapotocky, L. Ramos, P. Poulin, T. C. Lubensky, and D. A. Weitz, Science **283**, 209 (1999).

[29] D. Pires, J.-B. Fleury, and Y. Galerne, Phys. Rev. Lett. **98**, 247801 (2007).

[30] M. Škarabot, M. Ravnik, S. Žumer, U. Tkalec, I. Poberaj, D. Babič, and I. Muševič, Phys. Rev. E **77**, 061706 (2008).

[31] R. P. Trivedi, I. I. Klevets, B. Senyuk, T. Lee, and I. I. Smalyukh, Proc. Natl. Acad. Sci. USA **109**, 4744 (2012).

[32] P. J. Ackerman, H. Mundoor, I. I. Smalyukh, and J. van de Lagemaat, ACS Nano **9**, 12392 (2015).

[33] B. Lee, S. Kim, J. Kim, and B. Lev, Sci. Rep. **7**, 15916 (2017).

[34] Y. Yuan, Q. Liu, B. Senyuk, and I. I. Smalyukh, Nature (London) **570**, 214 (2019).

[35] P.-G. de Gennes, Mol. Cryst. Liq. Cryst. **12**, 193 (1971).

[36] Y. Xie, Y. Li, G. Wei, Q. Liu, H. Mundoor, Z. Chen and I. I. Smalyukh, Nanoscale **10**, 4218 (2018).

[37] L. Wang and Y. Li, Chem. Mater. **19**, 727 (2007).

[38] G. H. Sheetah, Q. Liu, and I. I. Smalyukh, Opt. Lett. **41**, 4899 (2016).

[39] B. Abécassis, M. D. Tessier, P. Davidson, and B. Dubertret, Nano Lett. **14**, 710 (2014).

[40] P. G. de Gennes and J. Prost, *The Physics of Liquid Crystals*, 2nd ed. (Clarendon, Oxford, 1993).

[41] S. Chandrasekhar, *Liquid Crystals*, 2nd ed. (Cambridge University Press, Cambridge, 1992).

[42] H. Grebel, R. M. Hornreich, and S. Shtrikman, Phys. Rev. A **28**, 1114 (1983).

[43] J.-S. B. Tai and I. I. Smalyukh, Phys. Rev. E **101**, 042702 (2020).

[44] P. Oswald, J. Baudry, and S. Pirkl, Phys. Rep. **337**, 67 (2000).

[45] A. Carambassis, L. C. Jonker, P. Attard, and M. W. Rutland, Phys. Rev. Lett. **80**, 5357 (1998).

[46] R. F. Considine, R. A. Hayes, and R. G. Horn, Langmuir **15**, 1657 (1999).

[47] D. Andrienko, P. Patricio, and O. I. Vinogradova, J. Chem. Phys. **121**, 4414 (2004).

[48] H. Stark, J.-i. Fukuda, and H. Yokoyama, Phys. Rev. Lett. **92**, 205502 (2004).